Microstructure and strengthening mechanisms of 90W–7Ni–3Fe alloys prepared using laser melting deposition

Wang, Y.P.; Ma, S.Y.; Yang, X.S.; Zhou, Y.Z.; Liu, X.; Li, J.F.; Zhang, J.J.; Li, C.; Wang, X.Y.; Le, G. M.

Total number of authors:
11

Published in:
Journal of Alloys and Compounds

Link to article, DOI:
10.1016/j.jallcom.2020.155545

Publication date:
2020

Document Version
Peer reviewed version

Microstructure and strengthening mechanisms of 90W-7Ni-3Fe alloys prepared using laser melting deposition

Y.P. Wang[a,c], S. Y. Ma[a,c,d], X.S. Yang[a], X. Liu[a], J.F. Li[a], J.J.Zhang[a], C. Li[c], X.Y. Wang[a], G.M. Le[a,*], Y. Zhang[b,*]

[a] Institute of Materials, China Academy of Engineering Physics, Mianyang 621908, China

[b] Department of Mechanical Engineering, Technical University of Denmark, 2800 Kgs. Lyngby, Denmark

[c] Department of Materials Science and Engineering, College of Mechanical and Materials Engineering, North China University of Technology, Beijing 100144, China

[d] SLM Solutions (Shanghai) Co., Ltd., Shanghai 201100, China

*Corresponding authors at:

Institute of Materials, China Academy of Engineering Physics, Mianyang 621908, China. Tel.: +86 28 65726329. E-mail address: leguomin@126.com (G. Le)

Technical University of Denmark, Produktionstorvet, Building 425, room 214, 2800 Kgs. Lyngby, Denmark. E-mail address: yubz@mek.dtu.dk (Y. Zhang)

Abstract: The microstructure and mechanical properties of a 90W-7Ni-3Fe heavy alloy manufactured using laser melting deposition (LMD) have been investigated with a goal of understanding the LMD process and the relevant strengthening mechanisms. A reference sample prepared using liquid phase sintering (LPS) with similar composition has been used for comparison to isolate effects of the processing rate. The results show that the nearly fully-dense LMD sample consists of two periodically alternating sublayers containing different volume fractions of W particles. Compared to the reference LPS sample, the LMD sample has a higher W content in the binder matrix, a more refined microstructure, a higher dislocation density and a lower contiguity between W particles. Furthermore, the LMD sample has a yield strength of 822 $\pm$ 30 MPa, which is about 200 MPa higher than that of the reference LPS sample. This strength difference is quantitatively analyzed based on the microstructural observations. It is shown that the increased fraction of W-matrix interfaces, a higher interface bonding strength and more pronounced constraint effects, resulting from the higher processing temperature and fast cooling of LMD, provide extra strengthening. The present study provides an important basis for optimizing the LMD process for manufacture of high W content tungsten heavy alloys with improved mechanical properties.

Key Words: refractory metals, laser deposition, composites, microstructure, mechanical property

1. Introduction

Tungsten heavy alloys (WHAs) are widely used in the aerospace and nuclear industries as weight balances and radiation shielding, due to their high density, high strength, and good ductility [1, 2]. WHAs are conventionally prepared by liquid phase sintering (LPS) using blended elemental powders of W, Ni, and Fe or Cu [2, 3]. The typical microstructure of WHAs produced by LPS consists of spheroidized W particles embedded in a Ni-based binder matrix [1, 2, 4]. The high sintering temperature as well as the slow heating (<1 K/s) and cooling rates (<10 K/s) of the LPS process, however, usually result in significant reprecipitation and growth of W particles/grains [5]. High hardness and high strength are thus obtained only after microstructure refinement by thermo-mechanical treatments, such as swaging [6-8], which prevents net-shape fabrication of WHAs using LPS.

Many new processing methods have recently been developed either to improve the wetting behavior by chemical alloying [5, 9] or to refine the microstructure by e.g. reducing the processing time [2, 10-16]. Among these methods, additive manufacturing (AM), using methods such as laser melting deposition (LMD) or selective laser melting (SLM), has attracted much interest due to its potential to allow near net-shape manufacturing of complex components directly from digital models [15-27]. The high energy density of the laser beam can heat up the powders quickly (typically in the order of 10^{-3}~10^{-1} s), while a small molten volume results in a fast cooling rate as the beam moves to the next local volume. The ultrafast heating and cooling rates of LMD and SLM (>10^3~10^4 K/s) can significantly reduce the time during which structural coarsening can occur. However, for SLM-processed WHAs, the combination of a relatively small melt pool (on the order of 100 μm) and very fast cooling rates (10^5~10^6 K/s) [28] can lead to lack of fusion, thereby resulting in a limited rearrangement of the W particles [16, 18, 20-23]. As such, even with the use of powder-preheating, the microstructure of SLM-processed WHAs often contains a non-uniform distribution of W particles and a large number of pores, which makes SLM-processed WHAs very brittle [16]. This problem can be remedied by use of the LMD process. LMD provides comparatively large melt pools (on the order of several millimeters) and comparatively lower cooling rates (10^3~10^4 K/s) during solidification [28]. This combination ensures a sufficient amount of liquid to provide a transport path for solution and reprecipitation processes and to bridge and allow rearrangement of the W particles, both of which

are beneficial for homogenizing the distribution of W particles and reducing the porosity [15, 25-27]. It has very recently been demonstrated that fully dense WHAs with W contents of up to 90 wt.% [29] and excellent mechanical properties can be prepared using LMD [27]. However, the strengthening mechanisms in such material has not been quantitatively understood, and in that regard information is also needed on how the fast heating and cooling rates in the LMD process affect the microstructural evolution, including the densification process, the W content remaining in the matrix, and the contiguity of W-W particle interfaces.

The aim of the present study is to characterize the microstructure and mechanical properties of a 90W-7Ni-3Fe alloy manufactured using LMD, to understand microstructure evolution during the LMD process and the related strengthening mechanisms. To better address the effects of the fast processing rate, a 90W-7Ni-3Fe sample is also prepared using conventional LPS and used as a reference. By comparing the microstructural parameters of the two samples, the microstructural evolution and strengthening mechanisms of the LMD sample are quantitatively analyzed.

2. Experimental Procedures

2.1 Powders

Raw W, Ni, and Fe powders with purities of 99.9% were used for the LMD process. The W particles have polygonal shapes and an average size of 52 μm, while the Ni and Fe powders are approximately spherical with average sizes of 22 μm and 131 μm, respectively (see Fig. 1). The oxygen contents of the W, Ni, and Fe powders were 381 ppm, 3520 ppm, and 440 ppm, respectively. Powders with a weight ratio of 90:7:3 for W:Ni:Fe were mixed and shaken using a three-axis shaker for 3 hours. The mixed powders were dried by heating at 80 °C for 2 hours in vacuum.

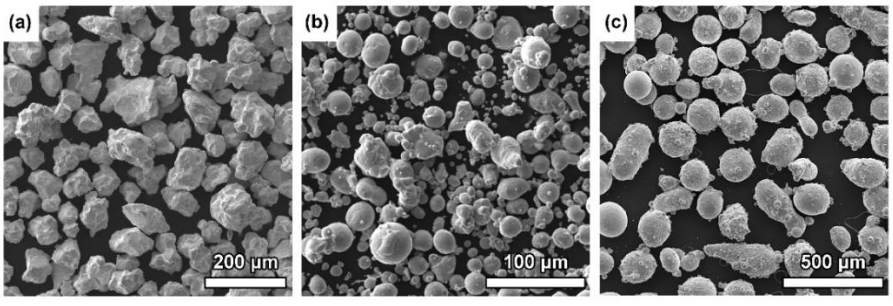

Fig. 1. SEM images of the powders: (a) W, (b) Ni, and (c) Fe.

2.2 LMD processing

An in-house developed LMD system was used to process the mixed powders. A schematic diagram of the system is shown in Fig. 2a. An ytterbium-doped fiber laser with a wavelength of 1070 nm and a spot diameter of approx. 2 mm was used to deposit the WHA on a 316L steel substrate. To avoid oxidation, the deposition process was carried out in a chamber filled with constantly flowing high purity argon, where the oxygen content was controlled to be below 20 ppm. The mixed powders were delivered into the chamber through a coaxial nozzle at a feeding rate of 10-15 g/min, under the protection of high purity argon. Further details about the LMD process can be found in Ref. [30].

Thin-wall plate samples with a thickness of ~3 mm, length of 55 mm, and height of ~40 mm were built layer-by-layer using a single laser scan with a power of 800 W and a speed of 400 mm/min. The height increment of each deposition layer was ~0.5 mm. The scanning direction for each new layer was reversed (see Fig. 2a).

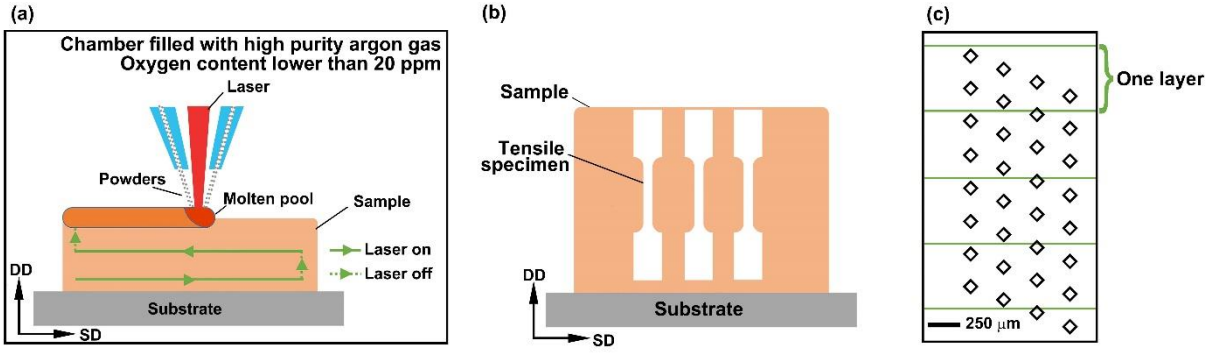

Fig. 2. Schematic diagrams showing (a) the LMD process for manufacturing thin-wall plate samples, (b) extraction of tensile specimens, and (c) the strategy for hardness indentations.

2.3 Reference LPS sample

A 90W-7Ni-3Fe alloy was also produced by conventional LPS as a reference. To promote good sintering, powders with a smaller size of 2–3 μm were mechanically alloyed by ball milling for 12 hours using WHA balls with a ball to powder weight ratio of 4: 1. The oxygen contents of the W, Ni, and Fe powders were 440 ppm, 670 ppm, and 2000 ppm, respectively. The mechanically alloyed powders were cold isostatically pressed at 180 MPa to obtain a cylindrical rod. The rod was sintered at a temperature of 1460 °C for 2 hours in vacuum, followed by furnace cooling.

2.4 Characterization of microstructure and mechanical properties

The microstructure and microzone chemistry were investigated on a cross-section of the LMD sample defined by the laser scanning direction (SD) and the deposition direction (DD) and on the LPS sample in a plane perpendicular to the cylindrical axis of the rod. The measurements were carried out using a Tescan Mira3 LMH field emission scanning electron microscope (SEM) equipped with an Oxford AZtec system for both electron backscatter diffraction (EBSD) and energy dispersive X-ray spectroscopy (EDS) analysis. For the EBSD orientation mapping, an electron accelerating voltage of 20 kV and a step size of 0.5 μm were used, while the EDS analysis was performed in point scan mode using an electron accelerating voltage of 20 kV, a beam intensity level of 13 and a count time of 180~300 s. Additionally, X-ray diffraction (XRD) analysis was performed using a DX-2700BH X-Ray diffractometer (Haoyuan Instrument Co., Ltd, Dandong, China) with a W filament operated at 40 kV and 40 mA and a fixed Cu anode ($\lambda_{k\alpha}$ = 0.154187 nm). The scan range was 30-110 ° with a step of 0.02 ° and a scanning speed of 2.4 °/min. The pores at the sample scale and the microstructure of the LMD sample were observed using a Nikon LV150N optical microscope and an Olympus SZ61 optical microscope, respectively. The porosity was determined from optical images using an in-house Matlab algorithm. The density of the samples was measured by Archimedes' method using a Mettler Toledo balance. The elemental impurity contents of C, S, O and N were analyzed by radio frequency gas extraction combustion coupled with infrared and thermal conductivity detectors using LECO analyzers (model CS344 for C/S elements and TC400 for O/N elements).

Dog-bone shaped specimens with a gauge length of 10 mm, a width of 2 mm, and a thickness of 1.6 mm were extracted for tensile tests. The tension direction was taken parallel to DD for the LMD sample (Fig. 2b), and to the cylindrical direction of the rod for the LPS sample. The tensile tests were performed using a Suns UTM5105 electronic universal tensile testing machine at a displacement rate of 0.4 mm/min (corresponding to an initial strain rate of approximately 6.7×10^{-4} s^{-1}). Three specimens were tested for each sample. The fracture surfaces were also characterized using the Tescan SEM. Microhardness testing was carried out using a HVS-1000A Vickers hardness instrument (Laizhou Huayin Testing Instrument Co., Ltd., Laizhou, China) with a diamond indenter under a load of 1000 g and a dwell time of 15 s. The indentation tests were conducted along four lines in an area containing four deposition layers on the cross-section for the LMD sample (see Fig. 2c) and at 5

random locations for the reference LPS sample.

3. Results

3.1 Phases

XRD results show that both the LMD sample and the reference LPS sample consist of two phases: BCC W and a FCC nickel-iron solid solution (see Fig. 3). No intermetallic phases were observed in either of the two samples.

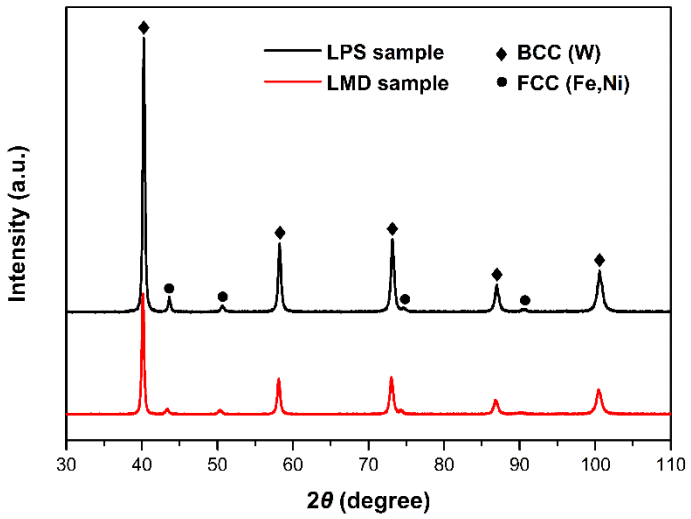

Fig. 3. XRD patterns of the LMD and reference LPS samples, showing the presence of identical phases of W and a nickel-iron solid solution in the two samples.

3.2 Microstructure

3.2.1 SEM and optical microscopy (OM)

SEM images show that the microstructure of the LMD sample is heterogeneous, consisting of alternating sublayers along DD each containing different volume fractions of W particles (see Fig. 4a). The sublayer at the top of each deposited layer has a low volume fraction of the W particles (hereafter termed a LW-sublayer), while the sublayer at the bottom has a high volume fraction (termed a HW-sublayer). The thickness of each LW-sublayer and HW-sublayer is about 200 µm and 300 µm, respectively — the sum of the two is equivalent to the height increment of each deposited layer. The volume fractions of the W particles are 79% and 88% in the LW- and HW-sublayers, respectively (see Table 1), leading to a total volume fraction of the W particles of 84.4%. The LW-

sublayers contain more, and larger (up to 200 μm), pores than the HW-sublayers (see Fig. 4b-d and Table 1). The total porosity of the LMD sample determined from OM images is about 0.99%.

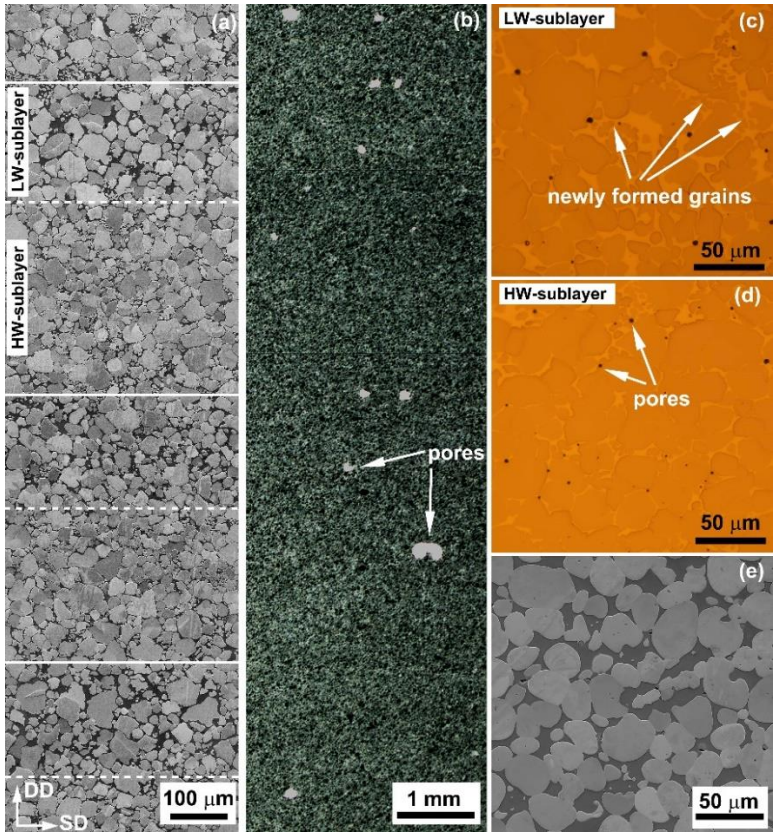

Fig. 4. SEM and OM images of the LMD and reference LPS samples. (a) SEM image showing the alternate sublayers with different volume fractions of W particles along DD in the LMD sample; (b) low and (c,d) high magnification OM images showing the size and distribution of pores as well as the microstructure of the LMD sample; (e) SEM image of the reference LPS sample, showing a fully-dense microstructure. In the SEM images, brighter regions are W particles, while darker regions are the binder matrix. In (b), the gray regions are the pores, while the rest is the alloy. In (c) and (d), the binder matrix appears brighter than the W particles.

Most of the W particles in the LMD sample retain their polygonal shape in both the LW- and HW-sublayers, inherited from the raw powders, though the corners are notably more round than in the raw powder. Within both the LW- and HW-sublayers, a large number of small W particles of approx. 5 μm are seen as well as a small fraction of dendrite-like features. The microstructure of the reference LPS sample is more homogenous (see Fig. 4e). The volume fraction of W particles in the reference LPS sample is 83%, slightly lower than that of the LMD sample.

The density of the LMD sample measured by Archimedes' method is 17.0 ± 0.24 g/cm^3. A porosity calculation based on comparing the measured density to the theoretical density of a 90W-7Ni-3Fe alloy (17.15 g/cm^3) yields a value of 0.87%, which agrees reasonably well with the measurement from OM analysis, indicating that the LMD samples are nearly fully-dense. The density for the reference LPS sample is 17.14 ± 0.15 g/cm^3.

Table 1. Microstructural parameters of the LMD and reference LPS samples.

	Thickness (μm)	Porosity* (%)	Volume fraction of W particles (%)	Contiguity of W particles	Median intercept length (μm)		W content in matrix (wt. %)
					W	matrix	
LMD LW-sublayer	204	0.36	79	0.22	10.5	2.2	29.4(±0.9)
LMD HW-sublayer	304	0.22	88	0.31	11.7	1.6	28.7(±1.9)
Reference LPS	-	-	83	0.34	15.5	3.5	26.8(±0.8)

*Only for pores with sizes smaller than 10 μm.

The contiguity (C_w) of the W particles is determined using equation (1):

$$C_W = \frac{2N_{WW}}{2N_{WW}+N_{WM}}, \quad (1)$$

where N_{WW} is the number of W-W contacts, and N_{WM} the number of W-matrix contacts. It is found that the contiguity of the W particles is smaller in both the HW- and LW-sublayers of the LMD sample than in the reference LPS sample. This is the case even though the volume fraction of the W particles in the HW-sublayers is higher than that of the reference LPS sample (see Table 1).

3.2.2 EBSD

Fig. 5 shows EBSD results for the LMD and reference LPS samples. Almost all the W particles are composed of a single grain for the reference LPS sample, whereas a small fraction of the W particles in the LMD sample contain 1 or 2 grain boundaries inside each particle. The median intercept length of the W grains is about 25% smaller in the LMD sample compared to the reference LPS sample (see Table 1), even though the starting W powders are >15 times larger for the LMD sample.

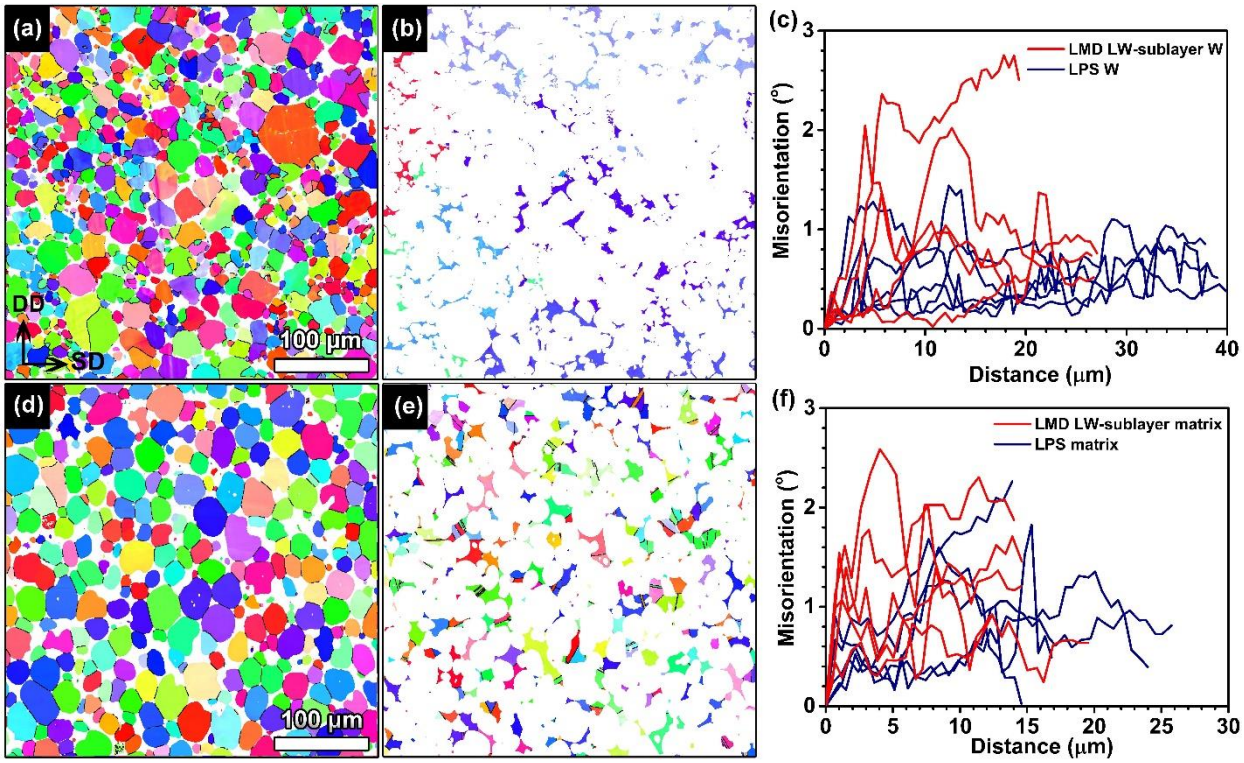

Fig. 5. EBSD results showing the microstructures of the LMD and reference LPS samples: (a) and (d) inverse pole figure (IPF) maps of the W phases in the LW-sublayer of the LMD sample and reference LPS sample, respectively; (b) and (e) IPF maps of the matrix in the LW-sublayer of the LMD sample and the reference LPS sample, respectively; (c) and (f) accumulative misorientations within 5 randomly-chosen W and matrix grains, respectively for each sample. Black lines in the IPF maps show grain boundaries with misorientations larger than 10°. The colors in the IPF maps represent crystallographic orientations along DD for the LMD sample and along the vertical axis of the map for the reference LPS sample.

There are many non-contiguous matrix regions in the LMD sample with similar orientations (see Fig. 5b), suggesting that these are parts of grains likely to be connected in 3D. Although the size of these matrix 'colonies' is large (100 μm), the median intercept length of the matrix grains is rather small for the LMD sample (see Table 1). In contrast, the matrix grains in the reference LPS sample typically have orientations significantly different from their neighboring matrix grains.

The maximum accumulative misorientation within most LMD W grains is above 1°, and can be up to 2.8° (see examples in Fig. 5c). The accumulative misorientation within most reference LPS W grains is below 1°. The maximum accumulative misorientations within the matrix of the LMD and reference

LPS samples are similar, though the misorientation gradient is larger for the LMD sample in regions about a few microns from the interface (see Fig. 5f).

3.3 Chemical content

EDS analysis shows that the W content in the matrix in both the LW- and HW-sublayers of the LMD sample is slightly higher than that in the matrix of the reference LPS sample (see Table 1). The O, N, C and S contents are more or less similar for the two samples (see Table 2). It should be noted that the relatively high oxygen content in the reference LPS sample is because the sintering was conducted in vacuum, and not in a hydrogen atmosphere.

Table 2. Contents of O, N, C and S in the LMD and reference LPS samples (units of ppm).

	O	N	C	S
LMD sample	453	9	<50	<2
Reference LPS sample	500	<20	15	6

3.4 Mechanical properties

The presence of periodically alternating sublayers of the LMD sample is also revealed by microhardness measurements along DD (see Fig. 6). For these measurements the first indentation was taken in a LW-sublayer (see Fig. 2c). The distance between neighboring peak values is about 500 μm, which matches the thickness of each deposited layer. The highest microhardness in the HW-sublayers is about 76 HV higher than the lowest hardness in the LW-sublayers. This hardness difference is expected due to the difference in the volume fraction of the W particles and in the porosity. The average microhardness of the reference LPS sample is also given in Fig. 6 for comparison. It is seen that even the lowest hardness value in the LMD sample is about 70 HV higher than the average hardness of the reference LPS sample.

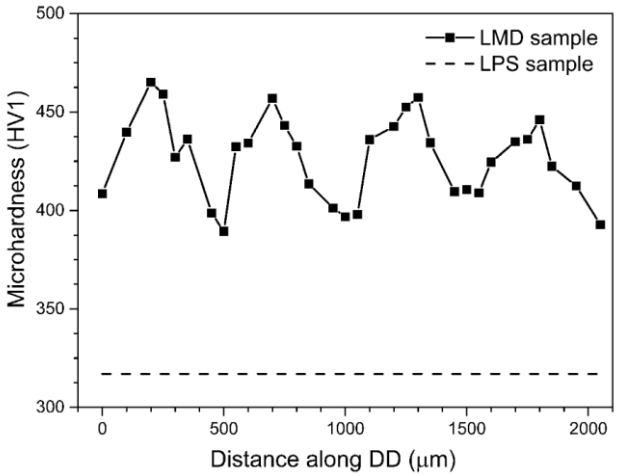

Fig. 6. Microhardness of the LMD and reference LPS samples. The microhardness of the LMD sample shows a periodic change along DD; the average microhardness of the reference LPS sample is indicated by the dashed line.

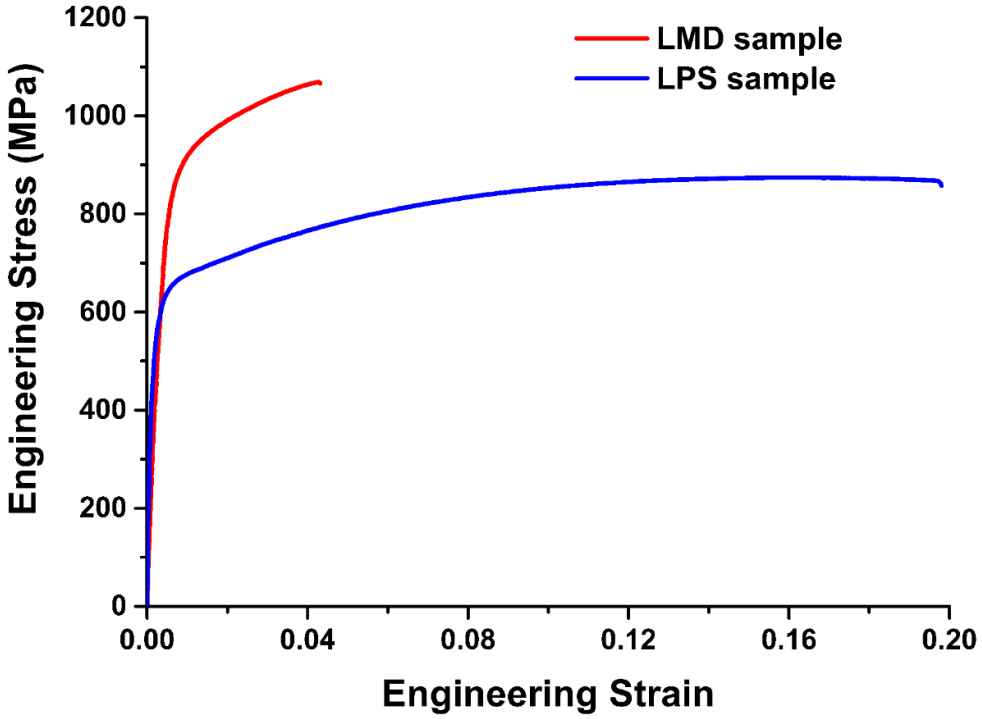

Fig. 7. Tensile tress-strain curves of the LMD and reference LPS samples.

Tensile stress-strain curves for the LMD and reference LPS samples are shown in Fig. 7. The LMD sample shows a much higher strength but a lower ductility than the reference LPS sample. The yield strength and tensile strength of the LMD sample reach 822 ± 30 MPa and 1037 ± 50 MPa,

respectively, both of which are about 150-200 MPa higher than those of the reference LPS sample (606 $\pm$ 4 MPa and 872 $\pm$ 14 MPa, respectively). The total elongation is 3.5 $\pm$ 0.7% and 18 $\pm$ 2% for the LMD and reference LPS samples, respectively.

3.5 Fracture surfaces

Fig. 8 shows fracture surfaces of the LMD and reference LPS samples. Some large pores with sizes of up to 200 μm are observed on the fracture surface of the LMD sample (see Fig. 8a), suggesting the fracture is likely to start at the large pores in the LW-sublayer. For the areas without pores, the fracture is dominated by cleavage of W particles and ductile tearing of the matrix (see Fig. 8b). For the reference LPS sample, pores are absent on the fracture surface (see Fig. 8c). In addition to cleavage of W particles and matrix ductile failure, W-W intergranular failure is also seen (examples are marked by arrows and labelled as W-W in Fig. 8d).

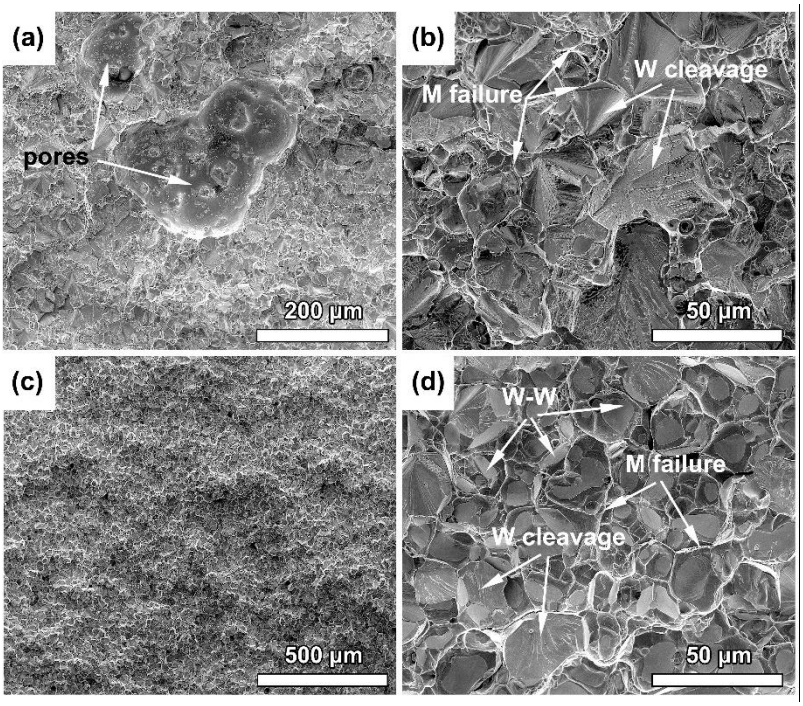

Fig. 8. SEM images showing fracture surfaces of the LMD sample (a, b) and reference LPS sample (c, d). Large pores are seen on the fracture surface of the LMD sample (a), and cleavage fracture features of W particles (W cleavage) as well as ductile dimple fracture features of matrix (M failure) are seen for both LMD and reference LPS samples (b and d). W-W intergranular grain boundary separations (W-W) are only visible in the reference LPS sample (d).

4. Discussion

4.1 LMD processing

The LPS process of WHAs consists of three stages of microstructural evolution [31]. The first stage involves the rearrangement of W particles. When the mixed powder is heated up to the processing temperature (1460 °C for the present case), the NiFe alloy melts, and the capillary force from liquid wetting acts as a driving force for rearrangement of the W particles. The second stage involves reprecipitation. W is dissolved in the NiFe liquid (finer particles and particle corners are favored) and upon cooling W reprecipitates on larger undissolved W particles, resulting in significant particle shape accommodation as well as pore elimination and grain growth. The final stage is solid-state sintering, where microstructural coarsening with very little densification takes place [1, 5, 31].

The LMD process involves similar processes, but takes place locally in a moving melt pool. The fast heating and cooling rates significantly accelerate the processes and lead to some unique microstructural features (see Figs. 4 and 5 and Table 1). These include: i) periodically alternating sublayers with different volume fractions of the W particles, ii) a relatively high W content in the matrix, iii) refined grains, iv) a larger orientation gradient in the W grains, v) a low contiguity of the W particles, and vi) large matrix ‘colonies’. As explained in the following the development of these features can be understood based on a consideration of the processing parameters.

During LMD, the high input energy laser can quickly (about 0.3 s) heat the powders to a high temperature. The highest temperature in the melt pool is higher than the processing temperature used for the reference LPS sample, 1460 °C, so that the NiFeW liquid solution has a lower viscosity, which allows heavier particles to deposit at the bottom of each layer under the force of gravity within a very limited time and leads to the observed layer separation behavior (i.e. feature i). The higher processing temperature of the melt can also dissolve a larger amount of W, which reduces the starting W particle size and increases the amount of liquid, and may possibly also lead to rounding of sharp corners of the particles, all of which can be beneficial for the rearrangement of W particles and contribute to the dense microstructure of the LMD sample. The larger matrix ‘colonies’ (feature vi) in the LMD sample (Fig. 5) is also a result of the larger amount of liquid. Additionally, the higher W solubility in the NiFeW solution can further reduce the solid-liquid interfacial energy between the

NiFeW solution and undissolved W particles, which promotes wetting of the W particles, and as such is beneficial for reducing the contiguity of the W particles (feature v) [4, 32]. The fact that many W particles are completely surrounded by a single matrix 'colony' (see Fig. 5) suggests that the larger amount of liquid may also contribute to the reduced contiguity.

As the laser moves to the next local volume, the fast cooling rate during solidification can reduce the time period for reprecipitation processes so that a larger amount of W can be preserved in the matrix (feature ii). The large fraction of small W grains in the LMD sample (Fig. 5) suggests that they may nucleate directly from the supersaturated solution due to the fast cooling rate.

After solidification, the faster cooling rate of LMD compared to the slow furnace cooling during LPS can further limit the extent of grain growth during solid-state cooling (feature iii). As a consequence, thermal stresses can develop during cooling in the composite because of the difference in coefficients of thermal expansion (CTE) between W and the NiFeW matrix (see Table 3) [14, 33]. The presence of W particles with a smaller CTE in a matrix with a larger CTE is likely to lead to compressive thermal stresses in both phases during solid-state cooling. These thermal stresses may lead to plastic deformation of both the W particles and the matrix during cooling from high temperature, which will relax the thermal stress to the yield stress of each phase at a given temperature [34, 35]. Additionally the fast cooling rate of the LMD process can lead to more plastic deformation and larger orientation gradients (feature iv) compared to the slow furnace cooling during the LPS process [36]. The distribution of the W particles (i.e. contiguity of W particles) may also affect the distribution of local thermal residual stress [34], which may further lead to different orientation gradients in the two phases (feature iv, see Fig. 5c and f). Last, but not least, the formation of intermetallic compounds can be avoided due to the fast cooling rate (see Fig. 3).

Table 3. Coefficients of thermal expansion (CTE) for W, Ni and Fe [33].

	CTE($\times 10^{-6}$/K)
W	4.5
Ni	13.0
Fe	11.8

4.2 Mechanical properties

Figure 9 shows a comparison of the mechanical properties of some 90W-7Ni-3Fe alloys processed by different methods. To eliminate the effects of strain rate, here only results obtained with strain rates similar to that used in the present study are included (i.e. quasi-static tensile tests at strain rates in the order of 10^{-4}~10^{-3} s^{-1}). Compared to SLM-processed WHAs [16, 23], LMD-produced WHAs can result in a better ductility. This is mainly because LMD provides larger melt pools than SLM, which helps to homogenize the microstructure and reduce the porosity. The strength of one of the data points for a SLM sample is higher than that of the present LMD sample, which is believed to be related primarily to the small reported powders/W grains of 4-11 μm in this sample [23], rather than a result of the processing route. It has been shown, for example, that if small powders are used an even higher strength can be obtained with LMD, while still retaining a uniform elongation of ~5% for a 75W-17.5Ni-7.5Fe alloy [27].

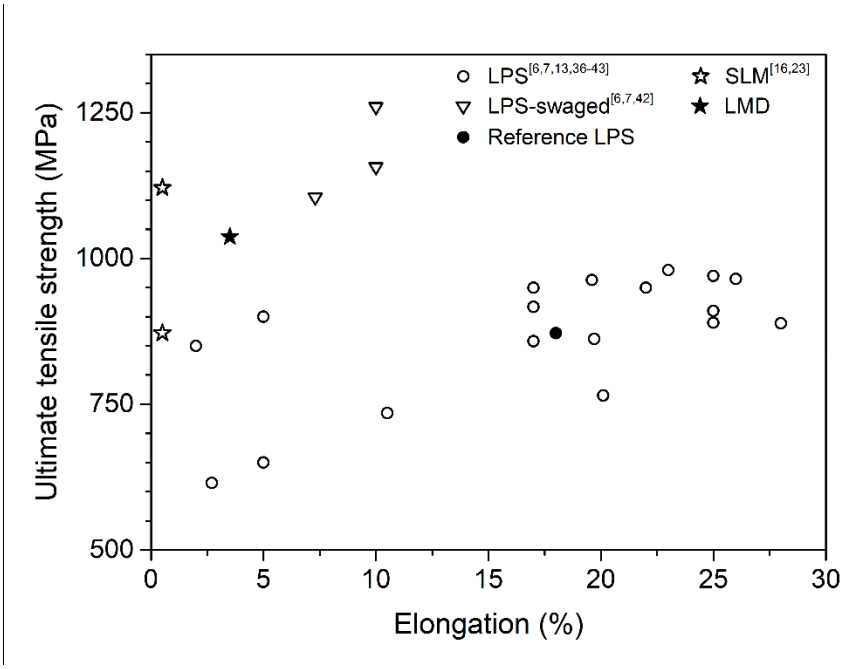

Fig. 9. Quasi-static tensile properties of the present LMD and reference LPS samples compared to other 90W-7Ni-3Fe alloys.

Compared to the reported as-sintered LPS samples [6, 7, 13, 37-44], LMD provides a higher tensile strength. Note that some of the LPS samples have higher strengths than the present reference LPS sample. Several factors may contribute to this, including the grain size, the matrix W content, and

the contiguity of W particles. However, as a quantitative analysis of the microstructure was not reported in these studies, it is not possible to draw any conclusions regarding the reasons for the strength difference. The strength of the LMD sample is close to that of some swaged LPS samples [6, 7, 43], the higher strength of which is mainly attributed to the additional plastic deformation after sintering. Such deformed samples have significantly different microstructures (including grain sizes, grain shapes, and interior dislocation densities) compared to the as-sintered samples. For the purposes of investigating the origin of the mechanical properties, it is therefore not appropriate to compare as-prepared samples to deformed materials.

To quantitatively understand the effects of the fast processing rates on the strengthening mechanisms of the LMD sample, the strength contributions from different microstructural parameters are estimated with respect to the present reference LPS sample. As the tensile direction is parallel to the deposition direction (see Fig. 2b), the weak links of the LW-sublayer regions in the LMD sample (see Figs. 6 and 7) are expected to control the tensile properties and are therefore quantified in detail below.

The yield strength of the composite can be calculated using a rule of mixtures calculation, i.e.

$$\sigma_{WHA} = f\sigma_p + (1-f)\sigma_m, \tag{2}$$

where f is the volume fraction of the W particles, and σ_p and σ_m are the strength of the W particles (p) and the matrix (m), respectively. Considering both the Hall-Petch strengthening and the dislocation strengthening, the strength of each phase can be calculated as:

$$\sigma_x = \sigma_x^0 + \frac{K_x}{\sqrt{d_x}} + M\alpha G_x b_x \sqrt{\rho_x}, \tag{3}$$

where σ_x^0 is the friction stress, K_x the Hall-Petch constant, d_x the grain intercept length, M the Taylor factor [45], α the dislocation interaction coefficient [46], G_x the shear modulus, b_x Burgers vector, ρ_x dislocation density, in which x represents p or m. For random textured BCC and FCC materials, M is close to 3 and α typically equals 0.24 [47-49]. The geometrical necessary dislocation (GND) density can be roughly estimated based on the orientation gradient (θ/d) using equation 4 [50]:

$$\rho = \frac{2}{b}\frac{\theta}{d}. \tag{4}$$

For the calculation, the value of θ/d is determined from the maximum accumulative misorientation within a grain and then averaged over 15 randomly chosen grains. It should be noted that this is likely to be an overestimate. Based on this calculations the estimated GND dislocation density in the W grains of the LMD sample is ~4 times that of the reference LPS sample (see Table 4). Using the parameters listed in Table 4 and the median intercept length as shown in Table 1 for the two phases, the strength increases for the LMD sample compared to the reference LPS sample due to the grain refinement and to the presence of dislocations are calculated to be 41 MPa and 52 MPa, respectively. It is rather difficult to estimate the effect of the W content increase in the matrix on the σ_m^0, but according to [51], a W concentration increase from 27% to 29% in the matrix can result in a total strength increase of ~20 MPa.

Table 4. Parameters used for quantification of strength of the LMD and reference LPS samples.

	K (MPa μm$^{1/2}$)	*G* (GPa)	*b*(nm)	Average orientation gradient (°/μm)		Dislocation density (×10^{12}m^{-2})	
				LMD	LPS	LMD	LPS
W	823 [52]	130	0.27	0.17	0.04	22.9	5.2
matrix	267 [53]	77	0.25	0.20	0.11	27.9	15.4

The calculated total increase of the yield strength for the LMD sample compared to the reference LPS sample is therefore about 113 MPa, which is at least ~100 MPa lower than the experimentally determined value. This mismatch may have a number of different sources. Within the large matrix 'colonies', the W particles are completely surrounded by one matrix grain; detrimental elements are less likely to be segregated at those interfaces due to the fast cooling rate [14]. Both factors may be beneficial for improving the interface bonding strength. Also a higher W content in the matrix in the LMD sample leads to a reduced strength difference between the hard W particles and the soft NiFeW matrix. This reduced strength difference, together with the smaller contiguity of the W particles (i.e. a higher fraction of W-matrix interfaces) can modify the constraint effect between the hard and soft phases (i.e. a strain accommodation between the larger plastic strain in the soft matrix and smaller strain in the hard W phase can give rise to slip on supplementary slip systems) and provide an extra strengthening [54]. In addition, the larger orientation gradients at the interfaces of the LMD sample (see Fig. 5c, f) may also have an impact on the constraint effects. A detailed quantification of these effects requires characterization of local residual strain (both plastic and elastic) using advanced

techniques, e.g. synchrotron micro-diffraction [34], which is, however, out of the scope of the present study.

For LPS with slow cooling rates, impurities such as O, N, C and S tend to segregate at the W-matrix interfaces during solidification, which can lead to poor bond strength of the interfaces and result in low strength and embrittlement [14]. The relatively high oxygen content in both the LMD and reference LPS samples can further reduce the ductility (see Fig. 9). However, the oxygen content in the present LMD and reference LPS samples is comparable (see Table 2), suggesting that the high oxygen content is not the main reason for the property differences between the two samples. From the fracture surfaces, it is evident that the ductility of the LMD sample is limited mainly by the presence of large pores.

The oxygen content in the LMD sample is similar to that of the raw powders (see section 2 and Table 2), suggesting that the high oxygen content in the LMD sample is very likely to originate from the raw powders. The oxygen content is likely to be reduced by preheating the powders in a hydrogen atmosphere before the LMD process [55]. The formation of the pores may be related to the gas used to deliver the powders or lack of fusion problem [29]. These large porosities may be eliminated by optimizing the processing parameters, e.g. input laser power, deposition layer thickness, scanning speed and powder shape, all which will be studied in the near future.

5. Conclusions

In this study the microstructure and mechanical properties of a dense tungsten heavy alloy (WHA) prepared using laser melting deposition (LMD) have been characterized using microscopy and hardness as well as tensile tests. It is found that LMD with high laser energy is a promising method for fabricating dense WHAs with a high W content of 90 wt.%. The main conclusions are:

i) The LMD processed WHAs consist of periodically alternating sublayers with different volume fractions of the W particles along the deposition direction. Within each deposited layer, the sublayer with a lower volume fraction of W particles is above the sublayer with a higher volume fraction. The maximum hardness difference between the two sublayers is about 75 HV.

ii) The LMD processed WHAs are 99% dense. A few large pores with size up to 200 μm are

observed, located mainly at the deposition layer interfaces. Within each deposited layer, the porosity in the top sublayer is slightly larger than that in the bottom sublayer.

iii) The yield and tensile strengths of the LMD processed WHA are 822 ± 30 MPa and 1037 ± 50 MPa. The ductility of the LMD sample is currently limited by the large pores formed during deposition.

iv) The fast heating and cooling rates during LMD leads to a refined microstructure, a relatively homogeneous microstructure (with lower contiguity of W particles), stronger interface bonding and a stronger binder matrix with supersaturated W content, all of which contribute to the higher strength of the LMD processed WHAs. Compared to conventional liquid phase sintering, it is suggested that the fast cooling rate of the LMD process results in extra strengthening from enhanced constraint effects between the two phases.

Acknowledgment

The authors gratefully acknowledge support from the Science Challenge Project (No. TZ2018006-0303-02), the National Natural Science Foundation of China (Grant No. 51871203), and Beijing Education Committee NCUT Basic Scientific Research Project, and Beijing Scientific and Technological Innovation Service Capacity Building Project. YZ acknowledges support from the European Research Council (ERC) under the European Union's Horizon 2020 research and innovation programme (grant agreement No 788567, M4D). Prof. Dorte Juul Jensen, Prof. Andy Godfrey, and Dr. Oleg Mishin are acknowledged for their valuable comments on the manuscript.

References

[1] W.D. Cai, Y. Li, R.J. Dowding, F.A. Mohamed, E.J. Lavernia, A review of tungsten-based alloys as kinetic energy penetrator materials, Review in Paticulate Materials 3 (1995) 71-131.
[2] N. Senthilnathan, A. Raja Annamalai, G. Venkatachalam, Sintering of Tungsten and Tungsten Heavy Alloys of W–Ni–Fe and W–Ni–Cu: A Review, Transactions of the Indian Institute of Metals 70 (2017) 1161-1176.
[3] R.M. German, Liquid Phase Sintering, Plenum Press, New York, 1985.
[4] R.M. German, P. Suri, S.J. Park, Review: liquid phase sintering, Journal of Materials Science 44 (2009) 1-39.
[5] A. Bose, R. Sadangi, R.M. German, A review on alloying in tungsten heavy alloys, Supplemental Proceedings, Volume 1: Materials Processing and Interfaces, TMS (2012) 455-465.
[6] N.K. Çalışkan, N. Durlu, Ş. Bor, Swaging of liquid phase sintered 90W–7Ni–3Fe tungsten heavy alloy, Int. J. Refract. Met. Hard Mater. 36 (2013) 260-264.
[7] N. Durlu, N.K. Çalişkan, Ş. Bor, Effect of swaging on microstructure and tensile properties of W–Ni–Fe alloys, Int. J. Refract. Met. Hard Mater. 42 (2014) 126-131.
[8] U. Ravi Kiran, J. Kumar, V. Kumar, M. Sankaranarayana, G.V.S. Nageswara Rao, T.K. Nandy, Effect of cyclic heat

treatment and swaging on mechanical properties of the tungsten heavy alloys, Materials Science and Engineering: A 656 (2016) 256-265.
[9] S. Zhou, Y.-J. Liang, Y. Zhu, R. Jian, B. Wang, Y. Xue, et al., High entropy alloy: A promising matrix for high-performance tungsten heavy alloys, Journal of Alloys and Compounds 777 (2019) 1184-1190.
[10] N. Senthilnathan, A.R. Annamalai, G. Venkatachalam, Microstructure and mechanical properties of spark plasma sintered tungsten heavy alloys, Materials Science and Engineering: A 710 (2018) 66-73.
[11] A. Mondal, A. Upadhyaya, D. Agrawal, Microwave and conventional sintering of 90W–7Ni–3Cu alloys with premixed and prealloyed binder phase, Materials Science and Engineering: A 527 (2010) 6870-6878.
[12] A. Upadhyaya, S.K. Tiwari, P. Mishra, Microwave sintering of W–Ni–Fe alloy, Scripta Materialia 56 (2007) 5-8.
[13] C. Zhou, J. Yi, S. Luo, Y. Peng, L. Li, G. Chen, Effect of heating rate on the microwave sintered W–Ni–Fe heavy alloys, Journal of Alloys and Compounds 482 (2009) L6-L8.
[14] A. Kumari, G. Prabhu, M. Sankaranarayana, T.K. Nandy, Effect of solution treatment temperature and cooling rate on the mechanical properties of tungsten heavy alloy, Materials Science and Engineering: A 688 (2017) 225-236.
[15] G.Y. Wang, S.N. Gu, S. Yang, Microstructure and properties of tungsten heavy alloys fabricated by laser direct deposition, Mater. Sci. Technol. (2016).
[16] A. Iveković, M.L. Montero-Sistiaga, K. Vanmeensel, J.-P. Kruth, J. Vleugels, Effect of processing parameters on microstructure and properties of tungsten heavy alloys fabricated by SLM, Int. J. Refract. Met. Hard Mater. 82 (2019) 23-30.
[17] P.C. Collins, D.A. Brice, P. Samimi, I. Ghamarian, H.L. Fraser, Microstructural Control of Additively Manufactured Metallic Materials, Annual Review of Materials Research 46 (2016) 18.11-18.29.
[18] R.D. Li, J.H. Liu, Y.S. Shi, L. Zhang, M.Z. Du, Effects of processing parameters on rapid manufacturing 90W–7Ni–3Fe parts via selective laser melting, Powder Metall. 53 (2010) 310-317.
[19] D.Q. Zhang, Z.H. Liu, Q.Z. Cai, J.H. Liu, C.K. Chua, Influence of Ni content on microstructure of W–Ni alloy produced by selective laser melting, Int. J. Refract. Met. Hard Mater. 45 (2014) 15-22.
[20] X. Wang, M. Wraith, S. Burke, H. Rathbun, K. DeVlugt, Densification of W–Ni–Fe powders using laser sintering, Int. J. Refract. Met. Hard Mater. 56 (2016) 145-150.
[21] Anru Yan, Zhiyong Wang, Tiantian Yang, Yanling Wang, Zhihong Ma, Sintering densification behaviors and microstructural evolvement of W-Cu-Ni composite fabricated by selective laser sintering, Int J Adv Manuf Technol 90 (2017) 657-666.
[22] M. Wang, R. Li, T. Yuan, C. Chen, M. Zhang, Q. Weng, et al., Selective laser melting of W-Ni-Cu composite powder: Densification, microstructure evolution and nano-crystalline formation, Int. J. Refract. Met. Hard Mater. 70 (2018) 9-18.
[23] J. Li, Z. Wei, B. Zhou, Y. Wu, S.-G. Chen, Z. Sun, Densification, Microstructure and Properties of 90W-7Ni-3Fe Fabricated by Selective Laser Melting, Metals 9 (2019) 884.
[24] M. Zhong, W. Liu, G. Ning, L. Yang, Y. Chen, Laser direct manufacturing of tungsten nickel collimation component, Journal of Materials Processing Technology 147 (2004) 167-173.
[25] C. Li, S. Ma, X. Liu, J. Li, G. Le, Microstructures and properties of 80W-20Fe alloys prepared using laser melting deposition process, Int. J. Refract. Met. Hard Mater. 77 (2018) 113-119.
[26] G. Wang, X. Sun, M. Huang, Y. Qin, Y. Yao, S. Yang, Influence of processing parameters on the microstructure and tensile property of 85 W-15Ni produced by laser direct deposition, Int. J. Refract. Met. Hard Mater. 82 (2019) 227-233.
[27] S. Zhou, L. Wang, Y.-J. Liang, Y. Zhu, R. Jian, B. Wang, et al., A strategy to achieve high-strength WNiFe composite-like alloys with low W content by laser melting deposition, Materials & Design 190 (2020) 108554.
[28] T. DebRoy, H.L. Wei, J.S. Zuback, T. Mukherjee, J.W. Elmer, J.O. Milewski, et al., Additive manufacturing of metallic components – Process, structure and properties, Progress in Materials Science 92 (2018) 112-224.
[29] C. Li, Y. Wang, S. Ma, X. Yang, J. Li, Y. Zhou, et al., Densification, microstructural evolutions of 90W-7Ni-3Fe tungsten heavy alloys during laser melting deposition process, Int. J. Refract. Met. Hard Mater. 91 (2020) 105254.
[30] J. Li, S. Xiang, H. Luan, A. Amar, X. Liu, S. Lu, et al., Additive manufacturing of high-strength CrMnFeCoNi high-entropy alloys-based composites with WC addition, Journal of Materials Science & Technology 35 (2019) 2430-2434.
[31] G.H.S. Price, C.J. Smithells, S.V. Williams, Sintered alloys. part I -copper-nickel-tungsten alloys sintered with a liquid phase present, J. Inst. Metals 62 (1938) 239-264.
[32] R.M. German, L.L. Bourguignon, B.H. Rabin, Microstructure limitations of high tungsten content heavy alloys, Journal of Metals (1985) 36-39.
[33] https://en.wikipedia.org/wiki/Thermal_expansion.
[34] Y.B. Zhang, T. Andriollo, S. Fæster, R. Barabash, R. Xu, N. Tiedje, et al., Microstructure and residual elastic strain at graphite nodules in ductile cast iron analyzed by synchrotron X-ray microdiffraction, Acta Materialia 167 (2019) 221-230.
[35] Y.B. Zhang, T. Andriollo, S. Fæster, W. Liu, R.I. Barabash, Three-dimensional local residual stress and orientation

gradients near graphite nodules in ductile cast iron, Acta Materialia 121 (2016) 173-180.
[36] Y.B. Zhang, T. Yu, R. Xu, A. Godfrey, D. Juul Jensen, Local residual stress within recrystallizing grains in iron, (in preparation).
[37] C. Zhou, J. Yi, S. Luo, Sintering High Tungsten Content W-Ni-Fe Heavy Alloys by Microwave Radiation, Metallurgical & Materials Transactions. Part A 45 (2014) 455-463.
[38] A. Pathak, A. Panchal, T.K. Nandy, A.K. Singh, Ternary W-Ni-Fe tungsten heavy alloys: A first principles and experimental investigations, Int. J. Refract. Met. Hard Mater. 75 (2018) 43-49.
[39] I.V. Andreiev, Effect of the rate of cooling tungsten heavy alloys of the W–Ni–Fe type from the sintering temperature on the formation of their physico-mechanical properties, Journal of Superhard Materials 38 (2016) 185-189.
[40] G. Prabhu, N. Arvind Kumar, M. Sankaranarayana, T.K. Nandy, Tensile and impact properties of microwave sintered tungsten heavy alloys, Materials Science and Engineering: A 607 (2014) 63-70.
[41] A. Panchal, U. Ravi Kiran, T.K. Nandy, A.K. Singh, Tensile Flow Behavior of Tungsten Heavy Alloys Produced by CIPing and Gelcasting Routes, Metallurgical & Materials Transactions A 49A (2018) 2084-2098.
[42] Y. Yu, M. Zu, C. Ren, W. Zhang, Effect of Strain Rate on the Plastic Deformation and Fracture of 90W-7Ni-3Fe Alloy Prepared by Liquid-Phase Sintering, J. Mater. Eng. Perform. 27 (2018) 6606-6615.
[43] X. Gong, J.L. Fan, F. Ding, M. Song, B.Y. Huang, Effect of tungsten content on microstructure and quasi-static tensile fracture characteristics of rapidly hot-extruded W–Ni–Fe alloys, International Journal of Refractory Metals & Hard Materials 30 (2012) 71-77.
[44] S. Eroglu, T. Baykara, Effects of powder mixing technique and tungsten powder size on the properties of tungsten heavy alloys, Journal of Materials Processing Technology 103 (2000) 288-292.
[45] Q. Liu, X. Huang, D.J. Lloyd, N. Hansen, Microstructure and strength of commercial purity aluminium (AA 1200) cold-rolled to large strains, Acta Materialia 50 (2002) 3789-3802.
[46] N. Hansen, X. Huang, Microstructure and flow stress of polycrystals and single crystals, Acta Materialia 46 (1998) 1827-1836.
[47] X. Zhang, N. Hansen, Y. Gao, X. Huang, Hall–Petch and dislocation strengthening in graded nanostructured steel, Acta Materialia 60 (2012) 5933-5943.
[48] N. Hansen, Hall–Petch relation and boundary strengthening, Scripta Materialia 51 (2004) 801-806.
[49] R. Neuhaus, C.H. Schwink, On the flow stress of [100]- and [111]- oriented Cu-Mn single crystals: a transmission electron microscopy study, Philos. Mag. A 65 (1992) 1463-1484.
[50] Y.B. Zhang, R. Barabash, High Resolution Mapping of Orientation and Strain Gradients in Metals by Synchrotron 3D X-ray Laue Microdiffraction, Quantum beam science 3 (2019) 6.
[51] A. Kumari, M. Sankaranarayana, T.K. Nandy, On structure property correlation in high strength tungsten heavy alloys, Int. J. Refract. Met. Hard Mater. 67 (2017) 18-31.
[52] S. Bonk, J. Hoffmann, A. Hoffmann, J. Reiser, Cold rolled tungsten (W) plates and foils: Evolution of the tensile properties and their indication towards deformation mechanisms, Int. J. Refract. Met. Hard Mater. 70 (2018) 124-133.
[53] T. Yamasaki, P. Schloβmacher, K. Ehrlich, Y. Ogino, Formation of amorphous electrodeposited Ni-W alloys and their nanocrystallization, Nanostruct. Mater. 10 (1998) 375-388.
[54] Y.H. Wang, J.M. Kang, Y. Peng, T.S. Wang, N. Hansen, X. Huang, Hall-Petch strengthening in Fe-34.5Mn-0.04C steel cold-rolled, partially recrystallized and fully recrystallized, Scripta Materialia 155 (2018) 41-45.
[55] C. Wu, Preparation of ultrafine tungsten powders by in-situ hydrogen reduction of nano-needle violet tungsten oxide, Int. J. Refract. Met. Hard Mater. 29 (2011) 686-691.

Figure captions

Fig. 1. SEM images of the powders: (a) W, (b) Ni, and (c) Fe.

Fig. 2. Schematic diagrams showing (a) the LMD process for manufacturing thin-wall plate samples, (b) extraction of tensile specimens, and (c) the strategy for hardness indentations.

Fig. 3. XRD patterns of the LMD and reference LPS samples, showing the presence of identical phases of W and a nickel-iron solid solution in the two samples.

Fig. 4. SEM and OM images of the LMD and reference LPS samples. (a) SEM image showing the alternate sublayers with different volume fractions of W particles along DD in the LMD sample; (b) low and (c,d) high magnification OM images showing the size and distribution of pores as well as the microstructure of the LMD sample; (e) SEM image of the reference LPS sample, showing a fully-dense microstructure. In the SEM images, brighter regions are W particles, while darker regions are the binder matrix. In (b), the gray regions are the pores, while the rest is the alloy. In (c) and (d), the binder matrix appears brighter than the W particles.

Fig. 5. EBSD results showing the microstructures of the LMD and reference LPS samples: (a) and (d) inverse pole figure (IPF) maps of the W phases in the LW-sublayer of the LMD sample and reference LPS sample, respectively; (b) and (e) IPF maps of the matrix in the LW-sublayer of the LMD sample and the reference LPS sample, respectively; (c) and (f) accumulative misorientations within 5 randomly-chosen W and matrix grains, respectively for each sample. Black lines in the IPF maps show grain boundaries with misorientations larger than 10°. The colors in the IPF maps represent crystallographic orientations along DD for the LMD sample and along the vertical axis of the map for the reference LPS sample.

Fig. 6. Microhardness of the LMD and reference LPS samples. The microhardness of the LMD sample shows a periodic change along DD; the average microhardness of the reference LPS sample is indicated by the dashed line.

Fig. 7. Tensile tress-strain curves of the LMD and reference LPS samples.

Fig. 8. SEM images showing fracture surfaces of the LMD sample (a, b) and reference LPS sample (c, d). Large pores are seen on the fracture surface of the LMD sample (a), and cleavage fracture

features of W particles (W cleavage) as well as ductile dimple fracture features of matrix (M failure) are seen for both LMD and reference LPS samples (b and d). W-W intergranular grain boundary separations (W-W) are only visible in the reference LPS sample (d).

Fig. 9. Quasi-static tensile properties of the present LMD and reference LPS samples compared to other 90W-7Ni-3Fe alloys.